A miniature electrothermal thruster using microwave-excited microplasmas: Thrust measurement and its comparison with numerical analysis

Yoshinori Takao,[a] Koji Eriguchi, and Kouichi Ono[b]
Department of Aeronautics and Astronautics, Graduate School of Engineering, Kyoto University, Yoshida-Honmachi, Sakyo-ku, Kyoto 606-8501, Japan

(Received 28 December 2006; accepted 9 May 2007; published online 26 June 2007)

A microplasma thruster has been developed, consisting of a cylindrical microplasma source 10 mm long and 1.5 mm in inner diameter and a conical micronozzle 1.0–1.4 mm long with a throat of 0.12–0.2 mm in diameter. The feed or propellant gas employed is Ar at pressures of 10–100 kPa, and the surface-wave-excited plasma is established by 4.0 GHz microwaves at powers of <10 W. The thrust has been measured by a combination of target and pendulum methods, exhibiting the performance improved by discharging the plasma. The thrust obtained is 1.4 mN at an Ar gas flow rate of 60 SCCM (1.8 mg/s) and a microwave power of 6 W, giving a specific impulse of 79 s and a thrust efficiency of 8.7%. The thrust and specific impulse are 0.9 mN and 51 s, respectively, in cold-gas operation. A comparison with numerical analysis indicates that the pressure thrust contributes significantly to the total thrust at low gas flow rates, and that the micronozzle tends to have an isothermal wall rather than an adiabatic. © *2007 American Institute of Physics*.
[DOI: 10.1063/1.2749336]

I. INTRODUCTION

For space systems, there is an ongoing trend toward miniaturization of spacecraft to reduce the overall mission costs and greatly increase the launch rates. Reducing the scale of spacecraft decreases the launch costs, and simplifying the structure leads to short development periods. In addition, microspacecraft mission scenarios may be envisioned where the mission is accomplished by a fleet of several microspacecraft to decrease the mission risk. Such a high reliability, as well as low-cost performance, is one of the great advantages for microspacecraft because their repair is not readily done in space. To realize microspacecraft, reducing the scale of their components is of critical importance, including micropropulsion systems. Various microthrusters have been proposed for microspacecraft applications, being under significant development for station keeping (requiring a thrust of approximately millinewtons) and attitude control (approximately micronewtons) applications.[1,2] However, none of the microthrusters is well established until now.

In the present work, we propose an electrothermal-type microthruster using microwave-excited microplasmas, which is one of the applications of microplasma sources on which extensive research has recently been done.[3–9] Assuming that plasmas are excited by surface waves, the major feature of such plasmas is that microwaves penetrate into the plasma chamber along the plasma-dielectric interfaces even in the overdense mode and the electron heating occurs in a thin (a few millimeters deep or less) skin-depth layer, that is, most of the power is absorbed near the interfaces.[10–16] Such mechanism of the power deposition is a great advantage to generate plasmas in a limited space without magnetic-field confinement. These features would contribute to a simple structure and long-time operation, compared with other conventional thrusters, because the present thruster requires no electrodes, neutralizers, or magnets.

The microplasma thruster consists of a microplasma source and a micronozzle. The plasma source is composed of a cylindrical dielectric tube, covered with a grounded metal. Microwaves are injected into the plasma chamber through a coaxial cable and a metal rod antenna covered with a separate quartz tube,[13–16] where propellant gases, Ar in this study, are ionized and heated up in the pressure range from 10 to 100 kPa. Such high thermal energy is converted into directional kinetic energy through the micronozzle to produce the thrust required. In comparison with cold-gas flows, the plasma-discharging flows can yield much higher exhaust velocity, so that higher thrust and specific impulse can be obtained. It would take less time to reach a required velocity increment with higher thrust, and higher specific impulse would lead to fuel conservation.

One might imagine that electrostatic-type microthrusters have better performance than the thruster presently developed. Several microelectrostatic thrusters have already been presented, producing smaller thrust and higher specific impulse.[17–20] The present thruster, however, has a much more robust construction with lower power consumption owing to a simple and lightweight system. In addition, the thruster is much smaller than microwave electrothermal thrusters using an electromagnetic resonant cavity,[21,22] so that it is more practical for microspacecraft less than 10 kg.

On the basis of this concept, we developed a numerical model for design consideration and estimated the thrust performance,[23] conducted plasma diagnostics of the microplasma source,[24,25] and measured the thrust performance as a preliminary experiment.[26] The objective of this study is to

[a]Present address: THine Electronics, Inc., Wakamatsu Bldg. 6F, 3-3-6, Nihombashi-Honcho, Chuo-ku, Tokyo, 103-0023, Japan
[b]Electronic mail: ono@kuaero.kyoto-u.ac.jp

 © 2007 American Institute of Physics

Downloaded 27 Jun 2007 to 130.54.110.22. Redistribution subject to AIP license or copyright, see http://jap.aip.org/jap/copyright.jsp

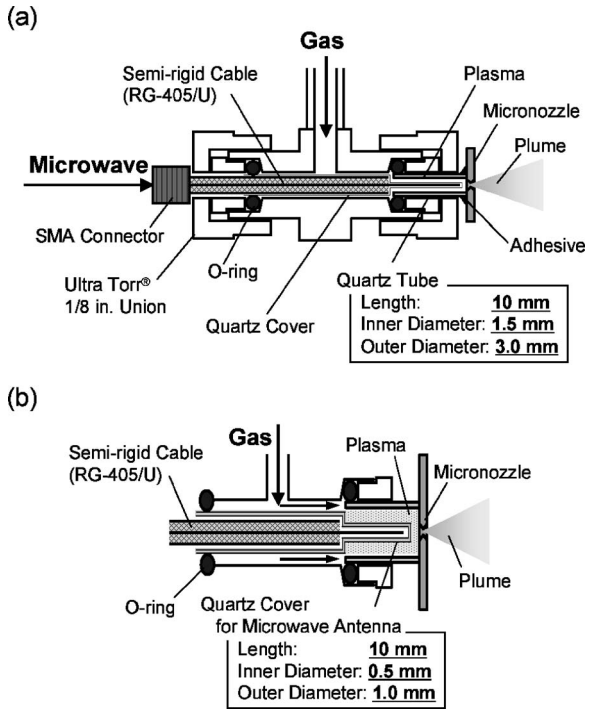


FIG. 1. (a) Cross-sectional view of the microplasma thruster presently developed, and (b) its radially enlarged view showing feed mechanisms of working gases.

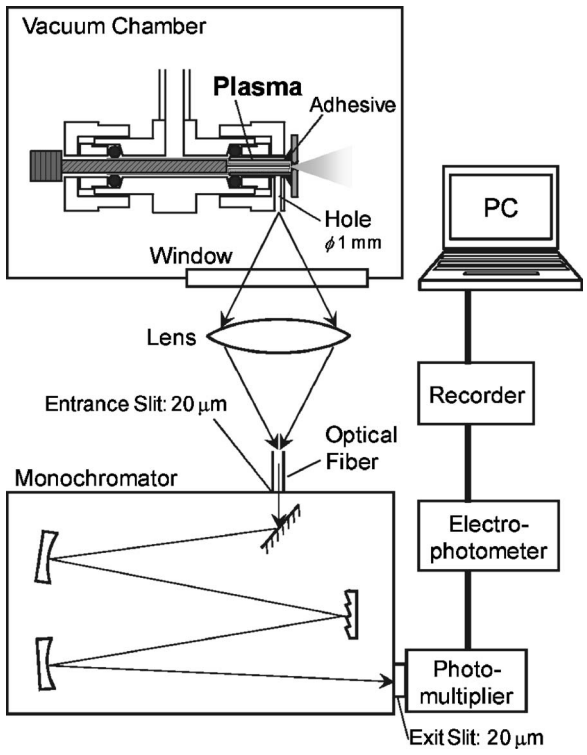


FIG. 2. Schematic diagram of the experimental setup for optical diagnostics of the microplasma source.

conduct a performance testing and to compare its result with a numerical analysis, to obtain more useful information about the microplasma thruster developed.

II. EXPERIMENTAL SETUP AND PROCEDURE

A. Microplasma source and micronozzle

Figure 1(a) shows a cross-sectional view of the microplasma thruster. The microplasma source is made of a straight quartz tube 10 mm in length, 1.5 mm in inner diameter, and 3.0 mm in outer diameter. A micronozzle is joined to one end of the tube with a ceramic adhesive. The center conductor of a semirigid coaxial cable (RG-405/U), protruding 10 mm beyond the insulator and outer conductor, is covered with a quartz tube and inserted into the plasma source as a microwave antenna, where the quartz tube is 10 mm in length, 0.5 mm in inner diameter, and 1.0 mm in outer diameter. Both the plasma source and antenna are inserted into a stainless steel Ultra-Torr vacuum fitting (Swagelok, SS-2-UT-6BT, 1/8 in. tube outer diameter) having a single hole on its side for gas feeding, to cover the microplasma source with a grounded metal. As shown in Fig. 1(b), both the quartz cover for the microwave antenna and the quartz tube of the plasma source are sealed with O rings, and propellant gases flow into the plasma source through the gap between the antenna and vacuum fitting.

Microwave signals of 4 GHz generated by an oscillator (Agilent Technologies, 8648D) are amplified through a four-stage semiconductor amplifier to powers of <10 W, and then fed through the semirigid coaxial cable into the microthruster. Working gases of Ar are also supplied to the thruster through a mass flow controller, where the plasma is generated with the help of an igniter. Here, the reflection of microwaves is simply suppressed by adjusting the cable length.

The critical electron density above which surface waves can propagate is about 9.5×10^{17} m^{-3} for a microwave frequency of 4 GHz with a dielectric constant of 3.8.[10–12] As in Ref. 25, the electron density measured by a Langmuir probe was in the range of 10^{17}–10^{19} m^{-3}, in the plasma jet plume downstream of the plasma source; the electron density may be larger about an order of magnitude in the microplasma chamber. The microplasma is probably sustained by surface waves, demonstrated by a numerical model.[15,16,23]

To estimate the gas temperature of the microplasma source, i.e., the reservoir temperature of the microthruster, a small amount of nitrogen is added to the argon plasma to observe the rotational spectra. Since electrons are inefficient in providing the rotational energy to molecules owing to their small mass, the population of rotational states is controlled by collisions with heavy particles. Therefore, the rotational temperature is an estimate of the heavy particle kinetic (gas) temperature.[8] Figure 2 shows a schematic diagram of the experimental setup for optical diagnostics of the microplasma source. A single hole 1.0 mm in diameter was made in the nut of the vacuum fitting. The emissions from the hole are collected by a lens and transmitted through an optical fiber to a monochromator.[25]

The micronozzle is fabricated using a micromachining process with a diamond drill. Figures 3(a)–3(d) show a typical example of a conical micronozzle fabricated in a quartz plate, together with cross-sectional and top views of three types of micronozzles taken with an optical microscope. Three micronozzles have different throat diameters and nozzle lengths with the same inlet and exit diameters, to

Downloaded 27 Jun 2007 to 130.54.110.22. Redistribution subject to AIP license or copyright, see http://jap.aip.org/jap/copyright.jsp

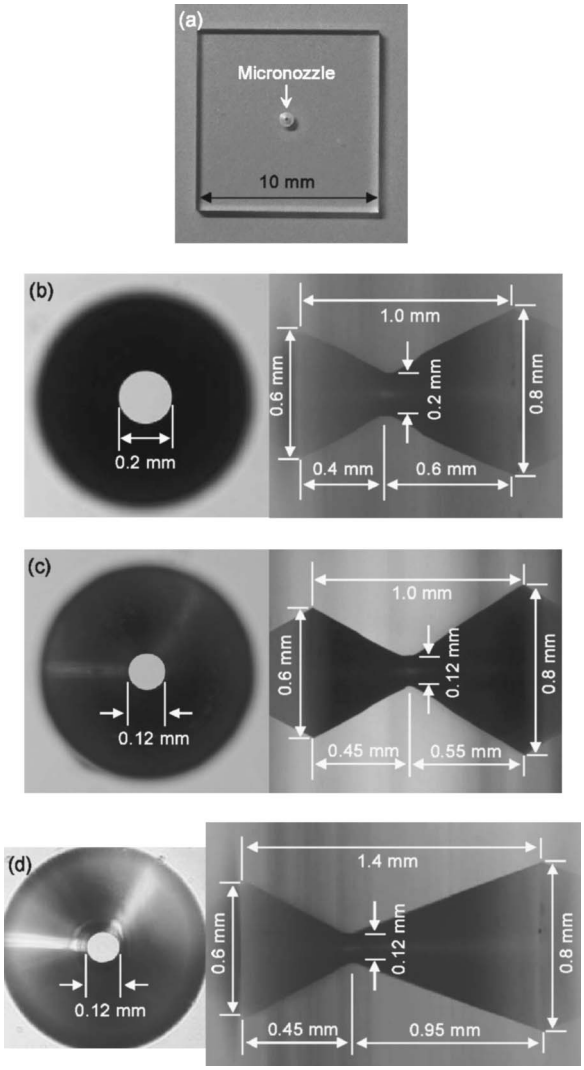


FIG. 3. Photograph images of (a) a conical micronozzle fabricated in a quartz plate and the cross-sectional and top views of three types of micronozzles: (b) throat diameter=0.2 mm and nozzle length=1.0 mm (ϕ200), (c) throat diameter=0.12 mm and nozzle length=1.0 mm (ϕ120t=1), and (d) throat diameter=0.12 mm and nozzle length=1.4 mm (ϕ120t=1.4).

investigate their geometric effect on the thrust performance. Here, we refer to the nozzle shown in Fig. 3(b) as ϕ200, the nozzle in Fig. 3(c) as ϕ120t=1, and the nozzle in Fig. 3(d) as ϕ120t=1.4 based on the respective dimensions. It should be noted that the minimum diameter of the diamond drill is 0.12 mm, so that the actual throat size of ϕ120t=1 and ϕ120t=1.4 is larger than 0.12 mm with an error of a few micrometers.

B. Thrust measurement

Figure 4(a) shows a schematic diagram of the experimental setup for measurement of the thrust performance. The plasma plume ejected from the thruster hits a cylindrical target, mounted on one end of a pendulum with some weights being on the other end for balance. The pendulum rotates around fulcrums of two knife edges without friction. The displacement of the pendulum is detected by a laser sensor (Keyence, LK-G85), where the resolution is about ±0.2 μm. The microthruster and pendulum are installed in a stainless

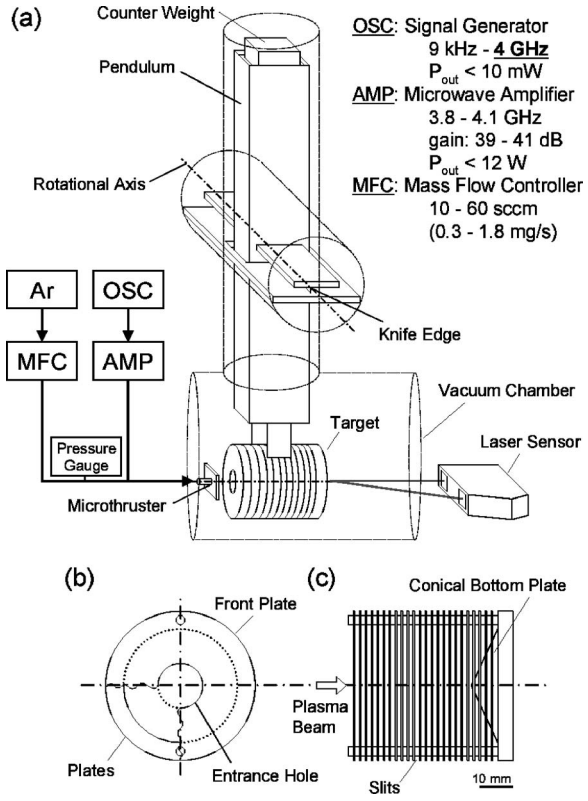


FIG. 4. (a) Schematic diagram of the experimental setup for thrust measurement. (b) Front and (c) side views of the cylindrical target made of Teflon.

steel vacuum chamber evacuated by a rotary and turbomolecular pump. A Bourdon tube pressure gauge positioned upstream of the microthruster is used for measurement of the feed gas pressure, to estimate the pressure inside the microplasma source, i.e., the inlet pressure of micronozzles.

Figures 4(b) and 4(c) show the front and side views of the cylindrical target, similar to the one made by Yanagi and Kimura.[27] The plasma beam comes into the target made of Teflon, through the entrance hole on the front plate. The bottom plate of the target is conically shaped, and most rebounding gas particles from the bottom plate leave radially from the target through a number of slits on the side of the cylinder; in practice, the total opening area normal to the side is much larger compared with the area of the entrance hole. Thus, it is expected that the effect of rebounding particles on thrust measurement is negligible with this target.

To measure the thrust performance, firstly the microthruster is mounted on the pendulum instead of the target, and then the displacement of the thruster in cold-gas operation is obtained as a function of mass flow rate. The relation between the displacement and force is calibrated in advance by hanging some small weights of 12.3–23.5 mg with a thin wire 10 μm in diameter. Then, the thrust in cold-gas operation is determined as a function of mass flow rate. This procedure is referred to as the pendulum method.[28–31] Secondly, the cylindrical target is mounted on the pendulum, as shown in Fig. 4(a), and the displacement of the target is measured as a function of mass flow rate in cold-gas operation. The calibration is also carried out in a similar manner to the pendulum method, and the thrust in cold-gas operation is deter-

Downloaded 27 Jun 2007 to 130.54.110.22. Redistribution subject to AIP license or copyright, see http://jap.aip.org/jap/copyright.jsp

mined as a function of mass flow rate using the target. This procedure is referred to as the target method.[27,32] To confirm the accuracy of the thrust measurement by the target method, we compare the thrust obtained by the pendulum method with that by the target method. After the difference between the thrust performances measured by the two methods is confirmed to be negligible, the thrust in plasma-discharging operation is obtained by the target method.

One might imagine that it is much easier and more accurate to measure the thrust by the pendulum method in plasma-discharging operation. However, microwaves are injected into the thruster through semirigid or flexible coaxial cables, which are much thicker and more rigid than those for dc and rf circuits. In addition, the microwave energy is easily converted into thermal energy during propagation through coaxial cables, and thus the thermal expansion of cables significantly degrades the signal-to-noise (S/N) ratio during the thrust measurement.

Once the thrust F_t is measured, the specific impulse I_{sp} is determined using the mass flow rate $\dot{m}$ and the standard acceleration of gravity g as[33]

$$I_{sp} = \frac{F_t}{\dot{m}g}. \tag{1}$$

In plasma-discharging operation, the thrust efficiency η is estimated from[34]

$$\eta = \frac{F_t^2}{2\dot{m}P + F_0^2}, \tag{2}$$

where F_t is the thrust in plasma-discharging operation, F_0 is the thrust in cold-gas operation, and P is the microwave power absorbed in the thruster.

The thrust measurement was conducted at least five times for each experiment. The symbols and error bars in the figures shown below represent the average and maximum/minimum values of measurement, respectively. Note that the error bars of the specific impulse have a tendency to become larger with decreasing mass flow rate, because the relative error of the mass flow rate resulting from the accuracy of the mass flow controller is larger at lower gas flow rates.

III. EXPERIMENTAL RESULTS

A comparison of the thrust performances evaluated by the pendulum and target methods was firstly conducted in cold-gas operation for three types of micronozzles: $\phi 200$, $\phi 120t=1$, and $\phi 120t=1.4$. The results indicated that there is little difference between the two methods with the difference below ±2%. This is smaller than the values of error bars, so that the accuracy of measurement of the target method is sufficient in cold-gas operation. Although there are still some uncertainties in the case of plasma-discharging operation because the direct comparison cannot be conducted, the difference in thrust performance between the two methods could be expected to be within the error of the measurement.

Figures 5(a) and 5(b) show the thrust and specific impulse in cold-gas operation as a function of gas flow rate for three types of micronozzles. While the thrust increases monotonically with increasing gas flow rate, the specific impulse remains almost constant at around 50 s, being independent of the gas flow rate for all micronozzles. The average values seem to be a little larger for micronozzles with smaller throat diameters. However, the difference is within the range of error bars, and there is no significant difference in thrust performance among three types of micronozzles.

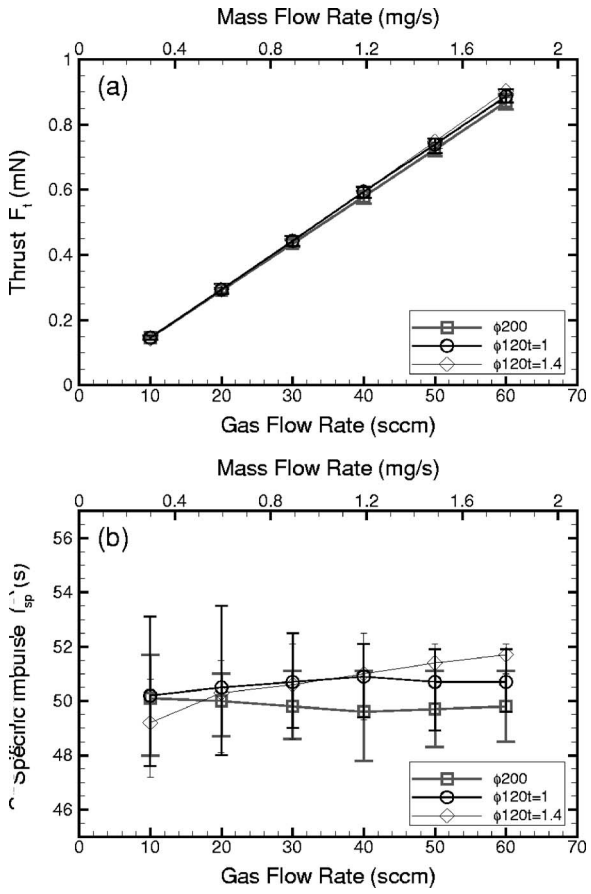


FIG. 5. (a) Thrust and (b) specific impulse in cold-gas operation, measured as a function of gas flow rate for three types of micronozzles: $\phi 200$, $\phi 120t=1$, and $\phi 120t=1.4$.

Figures 6(a)–6(d) show the photograph images of the microthruster in plasma-discharging operation with the micronozzle of $\phi 200$ under different operating conditions. We observe longer plasma plumes downstream of the micronozzle and stronger emission intensities in the microplasma source, with increasing Ar gas flow rate and microwave power. Stable plasma discharges were also confirmed during the operation within a few tens of minutes. Moreover, the quartz cover of the microwave antenna was found to have no damage after repetitive operations.

Figures 7(a) and 7(b) show the thrust and specific impulse in plasma-discharging operation as a function of gas flow rate for three types of micronozzles, measured at microwave powers of 3 and 6 W. The thrust performances are improved by discharging the plasma, increasing with increasing gas flow rate and microwave power. Compared with the results shown in Fig. 5(b), the specific impulse in plasma-discharging operation tends to increase with increasing gas flow rate. It can be seen that the difference in thrust performance among three micronozzles is insignificant within the error bars concerned. At a gas flow rate of 60 sccm (SCCM

Downloaded 27 Jun 2007 to 130.54.110.22. Redistribution subject to AIP license or copyright, see http://jap.aip.org/jap/copyright.jsp

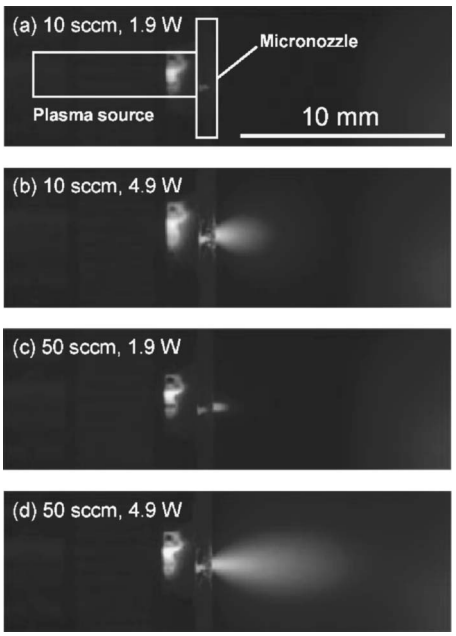


FIG. 6. Photograph images of the microthruster in plasma-discharging operation with the micronozzle $\phi 200$ under different operating conditions. The Ar gas flow rates and 4 GHz microwave powers are (a) 10 SCCM, 1.9 W; (b) 10 SCCM, 4.9 W; (c) 50 SCCM, 1.9 W; and (d) 50 SCCM, 4.9 W.

denotes cubic centimeter per minute at STP) (1.8 mg/s) for the micronozzle of $\phi 120t=1.4$, the thrust obtained is 1.2 mN at a microwave power of 3 W, giving a specific impulse of 66 s and a thrust efficiency of 12%; the thrust obtained is 1.4 mN at a microwave power of 6 W, giving a specific impulse of 79 s and a thrust efficiency of 8.7%, while the thrust and specific impulse are 0.9 mN and 51 s, respectively, in cold-gas operation. The thrust efficiency decreases with increasing microwave power, so that there is a trade-off between the fuel and power efficiencies. Although the specific impulse obtained is relatively low, the thrust obtained is of the order of millinewton at high gas flow rates, which could be used for a station-keeping maneuver for microspacecraft less than 10 kg.[1,2]

IV. NUMERICAL MODEL

It is complicated to develop a model for the entire part of the microthruster, and it is expected to be a time-consuming calculation even if a complete model is developed. Thus, we have developed a simple model for the micronozzle part to compare the experimental and numerical results. To describe the plasma flow inside the micronozzle, a two-temperature model is generally required, to give the temperature of electrons and heavy particles (neutrals and ions). However, it is impossible for the current setup to measure the electron density and temperature in the microplasma source, so that the electrons are not taken into account in the model assuming a calorically perfect gas. In practice, the plasma is treated as a nonionized high-temperature gas, and the model is employed for both cold-gas and plasma-discharging flows. Fortunately, since the particles contributing significantly to the thrust are not electrons but heavy particles, the effect of electrons on

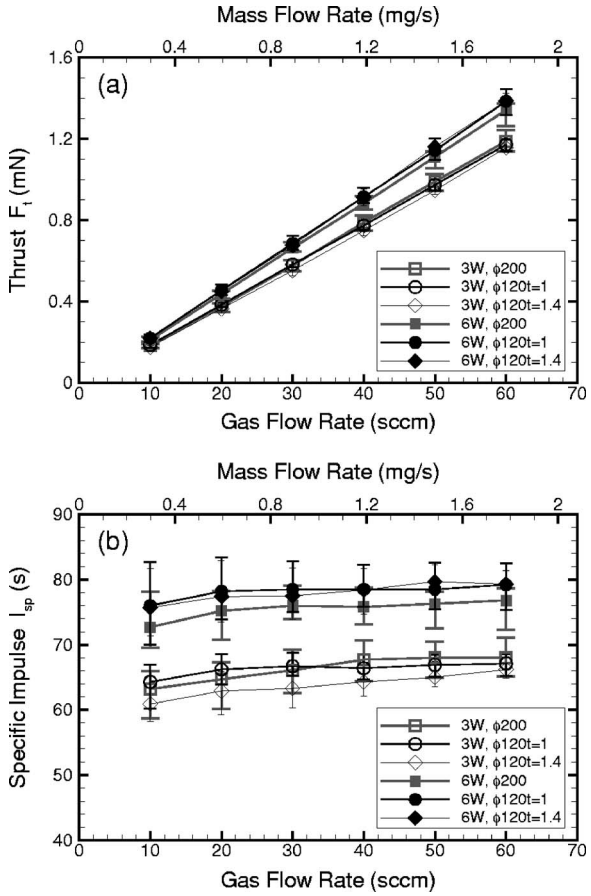


FIG. 7. (a) Thrust and (b) specific impulse in plasma-discharging operation, measured as a function of gas flow rate for three types of micronozzles: $\phi 200$, $\phi 120t=1$, and $\phi 120t=1.4$. Here, the microwave powers are 3 W (open symbols) and 6 W (closed symbols).

the flow fields could be negligible, and the model would give macroscopic parameters such as thrust and specific impulse.

The equations for the flow field inside micronozzles are the general compressive Navier-Stokes equations. The equations can be written in a conservative form as

$$\frac{d}{dt}\int\int\int \boldsymbol{Q}dV + \int\int \boldsymbol{F}_j dA_j = 0, \tag{3}$$

where $\boldsymbol{Q}=[\rho,\rho u,\rho v,E_t]^t$ is the vector of conservative variables to be solved, $\boldsymbol{F}_j$ is the inviscid/viscous flux vectors, V is the volume of a control volume, and A_j is the j component of the area vector $\boldsymbol{A}$ of the control volume. The total energy E_t is defined as

$$E_t = \rho\varepsilon + \frac{1}{2}\rho(u^2+v^2), \tag{4}$$

using the density ρ, axial velocity u, radial velocity v, and internal energy $\varepsilon=c_vT$, where T is the temperature and c_v is the specific heat at constant volume. The relation between the pressure p and internal energy ε is defined as $p=(\gamma-1)\rho\varepsilon$ with the ratio of specific heats $\gamma=5/3$ for Ar. The viscosity μ is evaluated from Sutherland's law:

Downloaded 27 Jun 2007 to 130.54.110.22. Redistribution subject to AIP license or copyright, see http://jap.aip.org/jap/copyright.jsp

$$\mu = \mu_0 \frac{T_0 + C}{T + C}\left(\frac{T}{T_0}\right)^{3/2}, \tag{5}$$

where $\mu_0 = 22.3 \times 10^{-6}$ Pa s and $T_0 = 293.15$ K are reference values at standard sea level, and $C = 142$ K is Sutherland's constant for Ar. Once the viscosity is obtained, the thermal conductivity κ can be calculated from

$$\kappa = \mu \frac{c_p}{P_r}, \tag{6}$$

where $P_r = 2/3$ is the Prandtl number for Ar and c_p is the specific heat at constant pressure.[35]

The Navier-Stokes equations are discretized by a finite volume approach, where the cell-centered scheme is employed, so that all flow properties are defined at the center of the control volume.[36–38] The inviscid fluxes at the cell boundary are evaluated using the modified advection upstream splitting method by pressure-based weight function (AUSM-PW+) scheme.[39] The space accuracy is kept to second order by the monotone upstream-centered scheme for conservation law (MUSCL) interpolation method.[40] For the viscous term, the usual central-average representation is used at the cell interface, so that all the diffusive terms is discretized in a central-difference fashion. The time integration is performed implicitly by lower-upper symmetric gauss-seidel (LU-SGS) method since it is robust and efficient.[41] The steady state solution is obtained as an asymptotic solution of the unsteady equations.

At the nozzle inlet, the flow is assumed to be subsonic, and hence one flow variable should be determined from the interior region. In cold-gas operation, the inlet temperature T_{in} is set at 300 K, and the mass flow rate $\dot{m}$ is taken to be the same as the experimental one. The radial velocity is set to be zero, and the axial velocity is obtained by extrapolation from the downstream point adjacent to the inlet.[35,42] The inlet density ρ_{in} is obtained from the mass flow rate and axial velocity, giving the static pressure p_{in} from the equation of state: $p_{\text{in}} = \rho_{\text{in}} R T_{\text{in}}$ with the gas constant R for Ar. In plasma-discharging operation, since the inlet temperature cannot be determined directly from the experiment, the static pressure is given to the system, which is assumed to be equal to the value of the pressure gauge. Here, the pressure has an error of ±1 kPa, because of the Bourdon gauge of the minimum scale of 10 kPa. The other inlet conditions are set in a similar manner to cold-gas operation.

At the nozzle wall, isothermal ($T_{\text{wall}} = 300$ K) and non-slip ($u = v = 0$) conditions are employed. At the nozzle exit, the flow velocity is supersonic for most part, but reduces to subsonic inside the boundary layer. In subsonic cases, one flow property should be determined outside the nozzle, and thus a small pressure value is specified thereat. In the case of supersonic, all flow properties are obtained from the zeroth extrapolation. Along the symmetric axis, the radial velocity component v is set at the opposite sign to the adjacent value, and the other properties are set equal to the corresponding adjacent values.

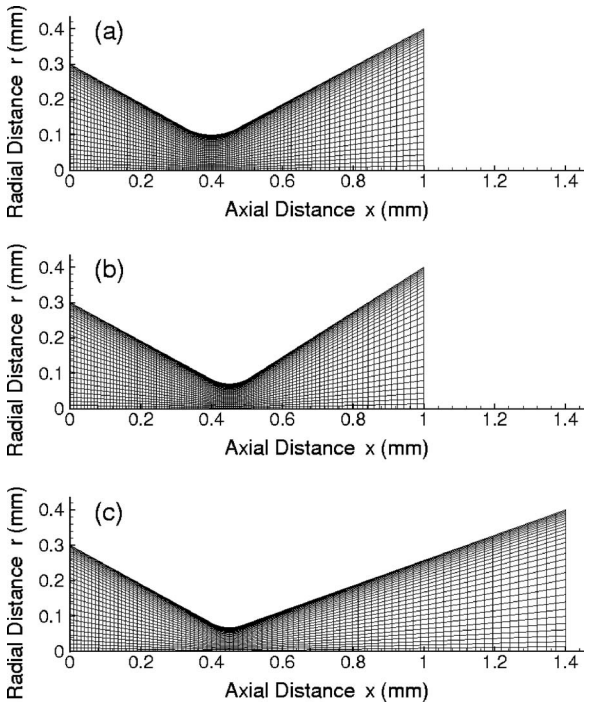


FIG. 8. Cross-sectional view and computational grids for three types of micronozzles: (a) $\phi 200$, (b) $\phi 120t = 1$, and (c) $\phi 120t = 1.4$. The simulation area of each nozzle is divided into 110 cells in the axial direction and 30 cells in the radial direction.

V. COMPARISON WITH NUMERICAL ANALYSIS

Figures 8(a)–8(c) show the cross-sectional view and computational grids for three types of micronozzles: $\phi 200$, $\phi 120t = 1$, and $\phi 120t = 1.4$, which are formed based on the nozzle configuration shown in Figs. 3(b)–3(d). The simulation area of each nozzle is divided into 110 cells in the axial direction and 30 cells in the radial direction, with the grid spacing being finer near the throat and the nozzle wall.

The throat diameter of the micronozzle has a significant effect on the flow properties; however, the direct measurement of the throat size cannot be conducted to an accuracy of 1 μm. To determine the throat diameter, several calculations with different throat sizes were performed for each micronozzle in cold-gas operation, and the inlet pressure calculated was compared with that measured by the Bourdon gauge. Figure 9 shows a comparison between the measured and calculated pressures for three types of micronozzles, where the error bars of the experimental data are due to the scale of the Bourdon pressure gauge. The numerical results are in good agreement with the experimental data, implying that the throat diameters are 0.2, 0.14, and 0.134 mm for three micronozzles of $\phi 200$, $\phi 120t = 1$, and $\phi 120t = 1.4$, respectively.

Figures 10(a) and 10(b) show the thrust and specific impulse in cold-gas operation as a function of gas flow rate, calculated for three types of micronozzles. Here, the thrust F_t and specific impulse I_{sp} are defined as

$$F_t = 2\pi \int_0^{r_{\text{ex}}} (\rho u^2 + p) r dr, \tag{7}$$

Downloaded 27 Jun 2007 to 130.54.110.22. Redistribution subject to AIP license or copyright, see http://jap.aip.org/jap/copyright.jsp

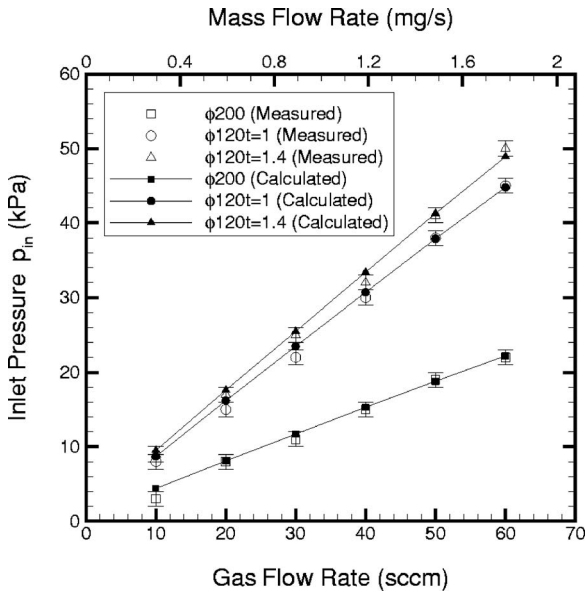


FIG. 9. Comparison between the measured and calculated inlet pressures in cold-gas operation for three types of micronozzles: $\phi 200$, $\phi 120t=1$, and $\phi 120t=1.4$.

$$I_{\mathrm{sp}} = F_t \left(g 2\pi \int_0^{r_{\mathrm{ex}}} \rho u r dr \right)^{-1} = \frac{F_t}{\dot{m} g}, \tag{8}$$

respectively, where r_{ex} is the exit radius of the nozzle.[42] The thrust increases monotonically with increasing gas flow rate,

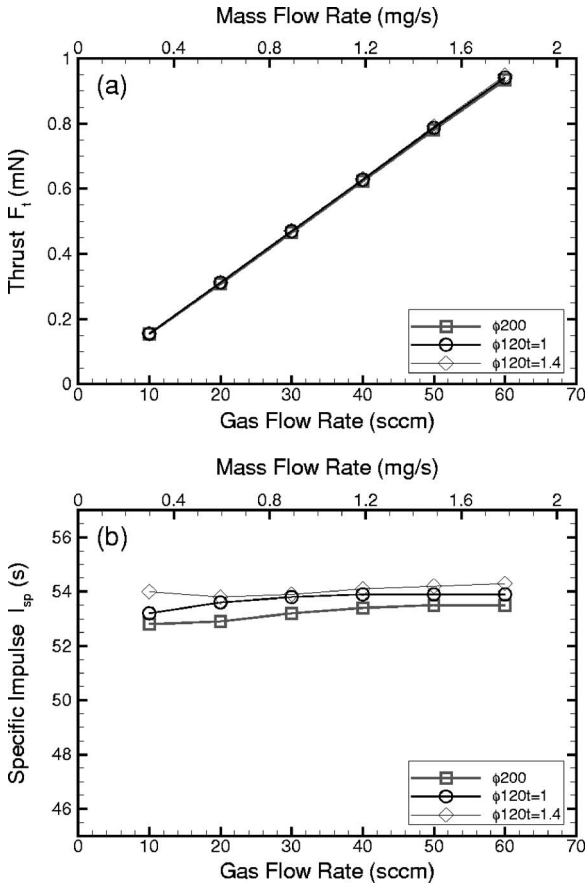


FIG. 10. (a) Thrust and (b) specific impulse in cold-gas operation, calculated as a function of gas flow rate for three types of micronozzles: $\phi 200$, $\phi 120t=1$, and $\phi 120t=1.4$.

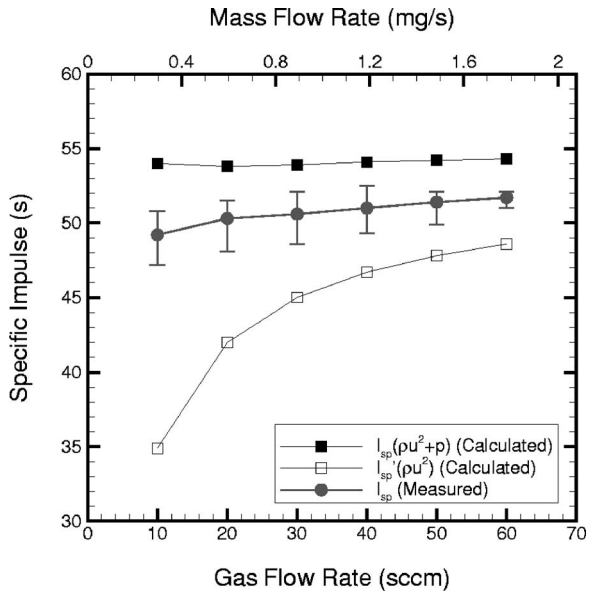


FIG. 11. Comparison between the measured and calculated specific impulses in cold-gas operation for the micronozzle $\phi 120t=1.4$. As for the specific impulse calculated, the one (I_{sp}) is that derived from the total or the momentum and pressure thrust, while the other (I'_{sp}) is that derived from the momentum thrust only.

where no significant difference is detected among three nozzles. The specific impulse exhibits a constant value of about 53 s, being independent of gas flow rate for all micronozzles. The numerical results also indicate that the micronozzles with smaller throat diameters give slightly larger specific impulses, which is consistent with the experimental data shown in Figs. 5(a) and 5(b), although the numerical values are larger than the experimental ones.

Figure 11 shows a comparison of the measured and calculated specific impulses in cold-gas operation for the micronozzle $\phi 120t=1.4$. Here, using the momentum thrust F'_t,

$$F'_t = 2\pi \int_0^{r_{\mathrm{ex}}} \rho u^2 r dr, \tag{9}$$

the specific impulse I'_{sp} is defined as

$$I'_{\mathrm{sp}} = F'_t \left(g 2\pi \int_0^{r_{\mathrm{ex}}} \rho u r dr \right)^{-1} = \frac{F'_t}{\dot{m} g}. \tag{10}$$

It is noted that F'_t is the momentum thrust only, whereas F_t in Eq. (7) consists of the momentum and pressure thrust. The specific impulse I'_{sp} increases with increasing gas flow rate, while the specific impulse I_{sp} remains almost constant; in practice, the numerical behavior of I_{sp} is in good agreement with the experimental data. These results can be explained in view of the flow fields inside the micronozzle as in Figs. 12(a) and 12(b), which show the Mach number contours at Ar gas flow rates of 10 and 60 SCCM. Although significant boundary layers occur at both gas flow rates, the layer is much thicker at 10 SCCM than that at 60 SCCM. Moreover, the maximum Mach number is observed inside the micronozzle, not at the nozzle exit, for 10 SCCM flows. Thus, it follows that the thicker boundary layers impede the flow expansion in the micronozzle at lower gas flow rates, where the nozzle flow is heavily underexpanded and higher pres-

Downloaded 27 Jun 2007 to 130.54.110.22. Redistribution subject to AIP license or copyright, see http://jap.aip.org/jap/copyright.jsp

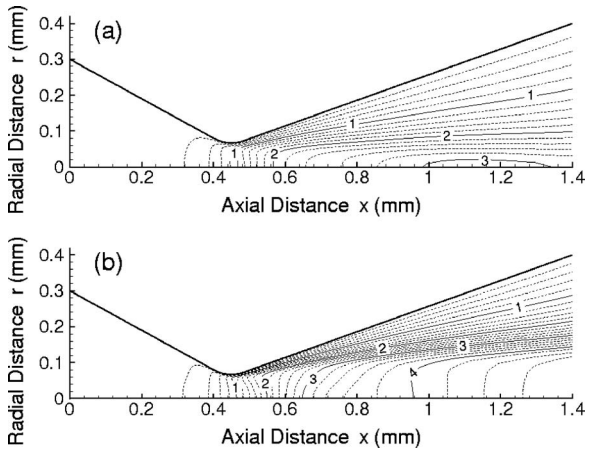


FIG. 12. Mach number contours in cold-gas operation for the micronozzle $\phi 120t=1.4$ at Ar gas flow rates of (a) 10 SCCM (0.30 mg/s) and (b) 60 SCCM (1.8 mg/s).

sures are obtained at the nozzle exit. Increasing the gas flow rate, in turn, alleviates these effects, leading to larger flow velocities and lower pressures at the nozzle exit, and hence to larger momentum thrust and smaller pressure thrust, which in turn results in the almost constant specific impulse I_{sp} in cold-gas operation. We thus conclude that the pressure thrust significantly contributes to the total thrust at low gas flow rates for the microthruster, as indicated in Ref. 23.

To calculate the thrust performance in plasma-discharging operation, the nozzle inlet pressure is required. As described earlier with respect to boundary conditions in the numerical model, the inlet pressure p_{in} is assumed to be equal to that measured by the Bourdon pressure gauge, which is summarized in Table I under different conditions for three types of micronozzles. Figures 13(a) and 13(b) show the thrust and specific impulse in plasma-discharging operation at microwave powers of 3 and 6 W, calculated using the pressures and mass flow rates in the table as nozzle inlet conditions for three micronozzles, where the error bars are derived from the error of the pressure p_{in}. The thrust performance increases with increasing gas flow rate and microwave power; the difference among three micronozzles is found to be insignificant within the error bars. These numerical results are consistent with the experiment data shown in

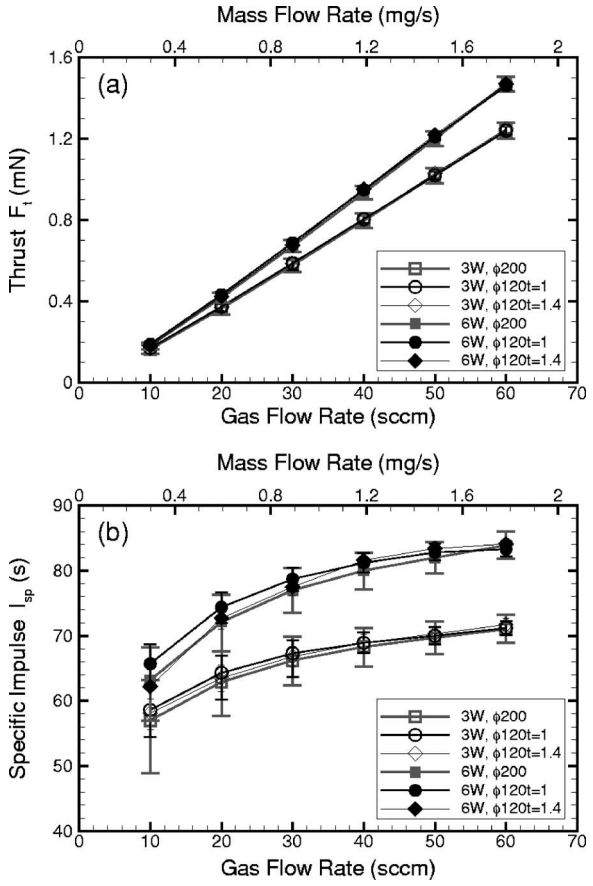


FIG. 13. (a) Thrust and (b) specific impulse in plasma-discharging operation, calculated as a function of gas flow rate at microwave powers of 3 W (open symbols) and 6 W (closed symbols) for three types of micronozzles: $\phi 200$, $\phi 120t=1$, and $\phi 120t=1.4$. Here, the error bars are those derived from the error of the inlet pressure p_{in} measured by the Bourdon tube pressure gauge.

Figs. 7(a) and 7(b). However, the specific impulse is underestimated at low gas flow rates while it is overestimated at high flow rates, as compared with the experiment; in practice, the discrepancy is larger at lower gas flow rates, where the Reynolds number in plasma-discharging operation is smaller than that in cold-gas operation, because of higher viscosities owing to increased gas temperatures. It appears that for micronozzle flows at low Reynolds numbers, the

TABLE I. Inlet pressure p_{in} measured by the Bourdon tube pressure gauge, at microwave powers of 3 and 6 W for different gas flow rates from 10 to 60 SCCM and for three types of micronozzles: (a) $\phi 200$, (b) $\phi 120t=1$, and (c) $\phi 120t=1.4$. Here, the pressure has an error of ±1 kPa because of the minimum scale of the pressure gauge.

	(a) $\phi 200$		(b) $\phi 120t=1$		(c) $\phi 120t=1.4$	
Ar (SCCM)	3 W p_{in} (kPa)	6 W p_{in} (kPa)	3 W p_{in} (kPa)	6 W p_{in} (kPa)	3 W p_{in} (kPa)	6 W p_{in} (kPa)
10	5±1	6±1	10±1	12±1	11±1	13±1
20	10±1	12±1	20±1	24±1	22±1	27±1
30	15±1	18±1	30±1	36±1	33±1	40±1
40	20±1	24±1	40±1	48±1	44±1	54±1
50	25±1	30±1	50±1	60±1	55±1	67±1
60	30±1	36±1	60±1	71±1	66±1	79±1

Downloaded 27 Jun 2007 to 130.54.110.22. Redistribution subject to AIP license or copyright, see http://jap.aip.org/jap/copyright.jsp

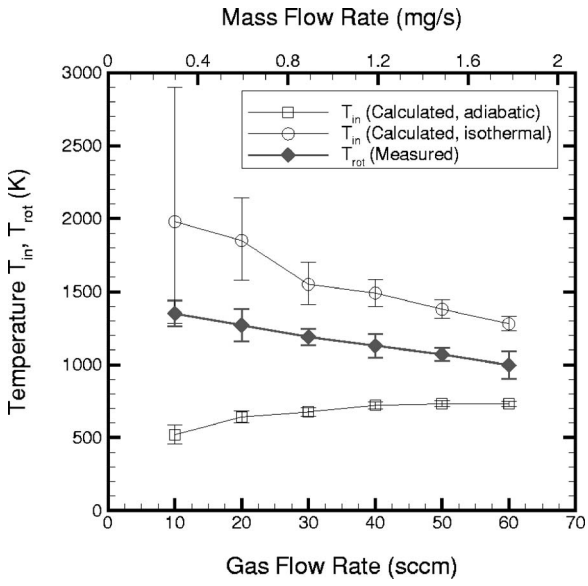


FIG. 14. Inlet temperatures T_{in} calculated under the adiabatic and isothermal wall conditions for the micronozzle $\phi 120t=1.4$ at a microwave power of 6 W, compared with the measured rotational temperature T_{rot} (N_2) of the microplasma source. Here, the error bars of the numerical T_{in} are those derived from the error of the inlet pressure p_{in} measured by the Bourdon tube pressure gauge, and the error bars of the experimental T_{rot} show the maximum/minimum values for five times measurements.

direct simulation Monte Carlo (DSMC) method gives more accurate results for macroscopic performance characteristics.[43] However, it is time consuming to use the DSMC method for the part from the inlet through throat, and so it would be better to employ a combined Navier-Stokes/DSMC approach.[44] In addition, an alternative approach is required to measure the thrust performance more accurately, for microthrusters in plasma-discharging operation. These are left for future work.

The numerical analysis conducted so far relies on the isothermal ($T_{wall}=300$ K) condition at the nozzle wall. However, there is no means of knowing the wall conditions directly. To investigate the effects of nozzle wall conditions, the calculation was also conducted using the adiabatic condition. Figure 14 shows the inlet temperatures T_{in} calculated under adiabatic and isothermal wall conditions for the micronozzle $\phi 120t=1.4$ at a microwave power of 6 W, together with the rotational temperature T_{rot} of the microplasma source measured at the same power by optical emission spectroscopy, as shown in Fig. 2. Here, the inlet temperature is that at the nozzle inlet on the symmetric axis, i.e., at the origin of the computational grids shown in Fig. 8(c). While the inlet temperature increases with increasing gas flow rate under the adiabatic wall condition, the temperature decreases under the isothermal condition. The rotational temperature, which should be close to the gas temperature at the nozzle inlet, also decreases with increasing gas flow rate, which is similar to that under the isothermal wall condition. It is reasonable that the gas temperature should decrease with increasing gas flow rate, because the microwave power per unit mass flow rate decreases with increasing flow rate at fixed powers. These imply that the micronozzle tends to have an isothermal wall rather than an adiabatic. In practice, the micronozzle is fabricated in a quartz plate, which has a much larger area compared with the micronozzle, as shown in Fig. 3(a), so that the quartz plate seems to play a role as a kind of heat sink although the quartz has a low thermal conductivity. The nozzle wall condition is important because the flow properties in the micronozzle are significantly affected by the condition, as discussed in Ref. 23. The results obtained here would be useful for more precise simulation.

VI. CONCLUSIONS

The thrust measurement of a miniature electrothermal thruster using microwave-excited microplasmas has been conducted and compared with numerical analysis. The experimental results show a thrust performance improved by discharging the plasma; the thrust and specific impulse obtained are 1.4 mN and 79 s, respectively, at an Ar gas flow rate of 60 SCCM (1.8 mg/s) and an input power of 6 W giving a thrust efficiency of 8.7%. The thrust level measured indicates that the microplasma thruster can reduce the propellant mass more than 30% as compared with a cold-gas thruster, in the so-called north-south station keeping for microspacecraft of 10 kg in geosynchronous earth orbit. In addition, varying the microwave power directly results in variable thrust performance, which is important for propulsion applications. Compared with electrostatic-type microthrusters, which are practically useless without plasma discharges, the present thruster yields the same thrust range and is equally useful even in cold-gas operation. Simply turning microwaves on and off would lead to two modes of operation.

A comparison with numerical analysis indicates that for the microthruster, the pressure thrust contributes significantly to the total thrust at low gas flow rates, which is consistent with the results in our previous paper.[23] The comparison also indicates that the micronozzle tends to have an isothermal wall rather than an adiabatic one. The implication would be useful for more precise simulation of micronozzle flows, because the flow properties in the micronozzle are significantly affected by the wall conditions.

ACKNOWLEDGMENTS

This work was supported by a Grant-in-Aid for Scientific Research from the Ministry of Education, Culture, Sports, Science and Technology, Japan. One of the authors (Y.T.) was supported by Research Fellowships of the Japan Society for the Promotion of Science for Young Scientists.

[1] J. Mueller, *Proceedings of the 33rd AIAA/ASME/SAE/ASEE Joint Propulsion Conference*, Seattle, WA, 1997 (American Institute of Aeronautics and Astronautics, Washington, DC, 1997), Paper No. AIAA-97-3058.
[2] J. Mueller, *Micropropulsion for Small Spacecraft*, edited by M. M. Micci and A. D. Ketsdever (American Institute of Aeronautics and Astronautics, Reston, 2000), Chap. 3.
[3] K. Terashima, L. Howald, H. Haefke, and H. Guntherodt, Thin Solid Films **281–282**, 634 (1996).
[4] H. Yoshiki and Y. Horiike, Jpn. J. Appl. Phys., Part 2 **40**, L360 (2001).
[5] J. Hopwood, O. Minayeva, and Y. Yin, J. Vac. Sci. Technol. B **18**, 2446 (2000).
[6] A. M. Bilgic, U. Engel, E. Voges, M. Kückelheim, and J. A. C. Broekaert, Plasma Sources Sci. Technol. **9**, 1 (2000).
[7] F. Iza and J. A. Hopwood, IEEE Trans. Plasma Sci. **31**, 782 (2003).

Downloaded 27 Jun 2007 to 130.54.110.22. Redistribution subject to AIP license or copyright, see http://jap.aip.org/jap/copyright.jsp

[8]F. Iza and J. A. Hopwood, IEEE Trans. Plasma Sci. **32**, 498 (2004).
[9]J. Kim and K. Terashima, Appl. Phys. Lett. **86**, 191504 (2005).
[10]M. Moisan and Z. Zakrzewski, J. Phys. D **24**, 1025 (1991).
[11]H. Sugai, I. Ghanashev, and M. Nagatsu, Plasma Sources Sci. Technol. **7**, 192 (1998).
[12]I. Ganachev and H. Sugai, Surf. Coat. Technol. **174–175**, 15 (2003).
[13]M. Tuda and K. Ono, J. Vac. Sci. Technol. A **16**, 2832 (1998).
[14]M. Tuda, K. Ono, H. Ootera, M. Tsuchihashi, M. Hanazaki, and T. Komemura, J. Vac. Sci. Technol. A **18**, 840 (2000).
[15]H. Kousaka and K. Ono, Jpn. J. Appl. Phys., Part 1 **41**, 2199 (2002).
[16]H. Kousaka and K. Ono, Plasma Sources Sci. Technol. **12**, 273 (2003).
[17]R. Wirz, R. Sullivan, J. Przybylowski, and M. Silva, *Proceedings of the 42nd AIAA/ASME/SAE/ASEE Joint Propulsion Conference*, Sacramento, CA, 2006 (American Institute of Aeronautics and Astronautics, Washington, DC, 2006), Paper No. AIAA-2006-4498.
[18]T. Ito and M. A. Cappelli, Appl. Phys. Lett. **89**, 061501 (2006).
[19]M. Tajmar, A. Genovese, and W. Steiger, J. Propul. Power **20**, 211 (2004).
[20]A. Dunaevsky, Y. Raitses, and N. J. Fisch, Appl. Phys. Lett. **88**, 251502 (2006).
[21]D. E. Clemens, M. M. Micci, and S. G. Bilén, *Proceedings of the 42nd AIAA/ASME/SAE/ASEE Joint Propulsion Conference*, Sacramento, CA, 2006 (American Institute of Aeronautics and Astronautics, Washington, DC, 2006), Paper No. AIAA-2006-5156.
[22]J. E. Brandenburg and M. E. Zooghby, *Proceedings of the 42nd AIAA/ASME/SAE/ASEE Joint Propulsion Conference*, Sacramento, CA, 2006 (American Institute of Aeronautics and Astronautics, Washington, DC, 2006), Paper No. AIAA-2006-5179.
[23]Y. Takao and K. Ono, Plasma Sources Sci. Technol. **15**, 211 (2006).
[24]Y. Takao, K. Ono, K. Takahashi, and Y. Setsuhara, Thin Solid Films **506–507**, 592 (2006).
[25]Y. Takao, K. Ono, K. Takahashi, and K. Eriguchi, Jpn. J. Appl. Phys., Part 1 **45**, 8235 (2006).
[26]Y. Takao, K. Ono, K. Takahashi, and K. Eriguchi, *Proceedings of the 29th International Electric Propulsion Conference*, Princeton, NJ, 2005 (The Electric Rocket Propulsion Society, Worthington, OH, 2005), Paper No. IEPC-2005-056.
[27]R. Yanagi and I. Kimura, J. Spacecr. Rockets **19**, 246 (1982).
[28]J. A. Burkhart, J. Spacecr. Rockets **8**, 240 (1971).
[29]T. W. Haag, Rev. Sci. Instrum. **62**, 1186 (1991).
[30]A. Sasoh and Y. Arakawa, Rev. Sci. Instrum. **64**, 719 (1993).
[31]S. Orieux, C. Rossi, and D. Estève, Rev. Sci. Instrum. **73**, 2694 (2002).
[32]R. Goldstein and F. N. Mastrup, AIAA J. **4**, 99 (1966).
[33]G. P. Sutton and O. Biblarz, *Rocket Propulsion Elements* (Wiley-Interscience, New York, 2001), Chap. 2.
[34]H. Tahara, K. Minami, T. Yasui, K. Onoe, Y. Tsubakishita, and T. Yoshikawa, Jpn. J. Appl. Phys., Part 1 **32**, 1822 (1993).
[35]J. D. Anderson, Jr., *Computational Fluid Dynamics: The Basics with Applications* (McGraw-Hill, New York, 1995).
[36]S. Kuchi-ishi and M. Nishida, *Proceedings of the 26th International Electric Propulsion Conference*, Kitakyushu, Japan, 1999 (The Electric Rocket Propulsion Society, Worthington, OH, 1999), Paper No. IEPC-99-029, p. 193.
[37]S. Kuchi-ishi and M. Nishida, *Proceedings of the 26th International Electric Propulsion Conference*, Kitakyushu, Japan, 1999 (The Electric Rocket Propulsion Society, Worthington, OH, 1999), Paper No. IEPC-99-044, p. 310.
[38]S. Kuchi-ishi, Ph.D. dissertation, Kyushu University, 1999.
[39]K. H. Kim, C. Kim, and O. H. Rho, J. Comput. Phys. **174**, 38 (2001).
[40]W. K. Anderson, J. L. Thomas, and B. V. Leer, AIAA J. **24**, 1453 (1986).
[41]S. Yoon and A. Jameson, AIAA J. **26**, 1025 (1988).
[42]S. C. Kim, J. Spacecr. Rockets **31**, 259 (1994).
[43]M. S. Ivanov, G. N. Markelov, A. D. Ketsdever, and D. C. Wadsworth, *Proceedings of the 37th Aerospace Sciences Meeting*, Reno, NV, 1999 (American Institute of Aeronautics and Astronautics, Washington, DC, 1999), Paper No. AIAA-99-0166.
[44]J. D. George and I. D. Boyd, *Proceedings of the 33rd Thermophysics Conference*, Norfolk, VA, 1999 (American Institute of Aeronautics and Astronautics, Washington, DC, 1999), Paper No. AIAA-99-3454.

Downloaded 27 Jun 2007 to 130.54.110.22. Redistribution subject to AIP license or copyright, see http://jap.aip.org/jap/copyright.jsp